Matching of 3D medical images with a potential based method

Grégoire Malandain, Jean-Marie Rocchisani

Rapports de Recherche

UNITÉ DE RECHERCHE
INRIA-SOPHIA ANTIPOLIS

N°1890

Programme 4

Robotique, Image et Vision

MATCHING OF 3D MEDICAL IMAGES WITH A POTENTIAL BASED METHOD

Grégoire MALANDAIN
Jean-Marie ROCCHISANI

Institut National
de Recherche
en Informatique
et en Automatique

2004 route des Lucioles
B.P. 93
06902 Sophia-Antipolis
France

Mars 1993

Abstract

Three dimensional (3D) images take an increasing importance in the medical imaging field. They may be produced by X-ray Computed Tomography (CT), Magnetic Resonance Imaging (MRI) or Positon Emitting Tomography (PET) for example. They usually contain complementary informations which have to be combined together in order to be useful to physicians. Combining the information of several 3D images sets the problem of the registration of these images. It arises when two images of the same modality are taken with different positions or taken at different times (before and after a surgery for example) or with two images of different modalities. We present a new method for computing the rigid transformation between two 3D objects. Our method looks like a gradient method that minimizes the distance between both objects, but is more powerful because it is in fact an application of the fundamental laws of dynamics which uses both first and second temporal derivatives of positions and allows an intuitive control of the minimization process. We show and discuss synthetic examples as well as real examples involving the registration of CT or MRI data of the head and the registration of PET and MRI images of the brain.

Index Terms: 3D matching, medical images registration, rigid transformation, potential minimization.

Résumé

Les images tridimensionnelles (3D) deviennent de plus en plus prépondérantes dans le domaine de l'imagerie médicale. Elles peuvent être produites par tomographie par rayons X (scanner X), imagerie par résonance magnétique (IRM) ou tomographie par émission de positons (TEP) par exemple. Elles contiennent des informations complémentaires qui doivent être fusionnées afin de fournir une aide précieuse aux practiciens. Combiner l'information de plusieurs images 3D pose le problème de la mise en correspondance de ces images. Il apparaît avec deux images de même modalité prises à des positions différentes ou à des instants différents (avant et aprés une opération par exemple) ou avec des images de modalités différentes. Nous présentons une nouvelle méthode de calcul de la transformation rigide entre deux objets 3D. Notre méthode ressemble à une descente de gradient qui minimise la distance entre les deux objets, mais elle est plus puissante car c'est en fait une application des lois fondamentales de la dynamique qui utilise les dérivées premières et secondes de la position par rapport au temps et permet un contrôle intuitif du processus de minimisation. Des résultats sur des données synthétiques et réelles sont présentés, comme la mise en correspondance de données scanner X ou IRM de la tête, ou la mise en correspondance d'images IRM et TEP du cerveau.

1 Introduction

Three dimensional (3D) images take an increasing and major importance in the medical imaging field. They may be produced by X-ray Computed Tomography (CT), Magnetic Resonance Imaging (MRI) or Positon Emitting Tomography (PET) for example. In order to follow and to quantify the evolution of a pathology, to locate the site of a metabolism, or to identify the anatomical structures with respect to an atlas, it becomes important to combine together several 3D images of the same part of the body.

Because of the extremely accurate quantitative results required by these application and the large volume of data to be processed, an automatic method of registration is necessary. Moreover, this registration has to be performed in 3D, simply because the protocols for image acquisition vary from one image modality to another, and also because even between two images of the same modality, the position of the patient is seldom perfectly known with respect to the acquisition device. It is therefore necessary to design a completely automatic 3D registration procedure.

Functions with respect to voxel intensity have been proposed to maximize a similarity index [27] or to minimize the variance of image ratio [34]. Those techniques give good results for PET or SPECT images but have not been applied to others images. As voxel intensity is obviously not invariant between images of different modalities, a first segmentation of images is necessary in order to obtain landmarks.

External markers (points on a stereotaxic frame or customized head holder which can be viewed in several modalities [13, 26, 35, 36]) or internal landmarks (some particular anatomical points, like blood vessel bifurcations [18]), have been widely studied. The transformation parameters are then computed by a classical method (for example, a least square method). Each method has its own disadvantages. External markers need the patient to carry a stereotaxic frame between both acquisitions. Moreover, the registration with older images is not possible. Internal landmarks often need a manual detection, whose accuracy depends on image resolution, and which has an effect on the computation of the transformation parameters. A local matching, based on crest lines, is described in [33]. It is a feature based method more robust to noise, resolution and anatomical variations, but it works only for good quality and high resolution images.

Instead of segmenting only a few particular points as the ones presented above, we prefer to look for a more significant part of the image like a complete organ (we use either the brain or the skull in the results we present). Because this segmentation can be imperfect or the considered landmark can be truncated, we are therefore looking for a 3D rigid registration

method allowing for occlusions. A preliminary segmentation method must yield two sets of points such that a significant subset of the first one can be rigidly superimposed on a subset of the second one[1].

Because of occlusions, a transformation between the two data sets cannot be sought globally, by superposing the centers of inertia, and aligning the axes of inertia for instance [1].

Many approaches for registration tolerating occlusions can be found in the literature of computer vision and robotics [2, 4, 15] and also in the medical field [16, 21, 25].

Because of the large number of points in a classical segmentation of a 3D image (e.g. the MRI image of the brain in figure 16 contains more than three millions points and the brain itself more than 400.000 points), prediction-verification, geometric hashing or Hough techniques as described in [2, 15, 16] are likely to be much too costly, with algorithms whose complexity is growing quadratic with the number of model points. On the contrary, methods based on potentials of attraction, like the ones described in [4, 19, 21, 25, 30] are potentially more economical, and we propose in this paper a new method of this type.

One of the image will create a potential of attraction, creating a dynamic evolution of the second image towards an "optimal" registration position. The originality stems from the original bases of the dynamic behavior of this system, which can be compared to the motion of a solid under the action of a potential field and offers a intuitive understanding of the minimization process.

We will discuss about the definition of the problem and the choice of the potential field. Then we present the matching flowchart and results on a synthetic object (which allow us to study the accuracy of the algorithm and its behavior with respect to local minima) and on real medical data. Details about mechanical elements and links with the transformation parameters are given in appendices.

2 Problem Formulation

In the formulation of the registration, two main problems arise. The first concerns the definition of the objects to register. The second is the choice of the technique which performs the registration.

The objects to register may be a set of scattered points (external or internal landmarks

[1] We assume that such a minimal segmentation procedure can always be found. This preliminary condition is much less restrictive than asking for a perfect segmentation of at least one of the images. Such methods have already been presented for the brain in [8, 14, 32] and also for other organs in [10]. In our results, 3D mathematical morphology is sufficient to treat all presented examples in a completely automatic process.

for instance), curves (like crest lines [33]), surfaces (shapes of organs) or volumes (organs themselves). The single condition which must be verified by both objects is that the chosen representation is compatible with the imaging modalities, i.e. that the same object exists in both images. In fact, the shape of the brain will be different in an anatomical imaging modality (like MRI) and in a metabolic imaging modality (PET for instance).

Because of this remark, we assume that we already have segmenting first the objects of interest (this segmentation will depend on images to register) which generalizes the problem.

The major contribution of our paper is to use the laws of mechanics to solve the registration problems, whereas other approaches are based on a static approaches. The idea is that the inertial properties of the system are a way to avoid local minima, and that this property can be controlled in a very intuitive way, due to our daily perception of mechanical events. The main idea of our approach is that any object subject to a potential field will exhibit motion derived from this field, and this motion leads to a minimum of potential.

2.1 Introduction

We prefer to deal with a potential because of its relation with energy. In fact, the potential will be directly related to the distance between objects, as we will see below, but we think that the potential approach is more appropriate to the formulation than the distance one. As an example, dealing with energy allows us to add to the potential any term we want (corresponding to some constraint we want to take into account) without changing the theoretical formulation (see [10] where the energy to minimize is made of several terms, each of them corresponding to one constraint).

We will then discuss the choice of the potential, the practical computation of the potential field, and the choice of the minimization process to use in order to find a minimum in the potential field.

In the following, we will refer to the object that creates the potential field as the *model*, and the object that will be subject to this potential as the *object*.

2.2 The Potential Field

To design a "good" potential field, we first state its desired properties. We identify two properties: first, the potential energy must be minimum when the *object* and the *model* are perfectly superimposed; second, the farthest the *object* from the *model* is, the greatest the potential energy must be.

In order to achieve the second property, we can choose a potential which is an increasing

function of the distance between the *object* and the *model*. The first property is then verified because the distance from the *model* to the *model* is equal to zero.

Let $d(M)$ be the distance between any point M and the closest *model* point P to M: $d(M) = \|\overrightarrow{MP}\|$. The first choice we can made for the potential field p is simply $p(M) = d(M)$. The problem is that the modulus of the gradient of the potential (which occurs in the minimization process) is always lesser than one. We prefer to have a modulus of the gradient which is an increasing function of the distance too. It will not change the convergence properties but it will speed up the minimization.

Let us then consider the potential field p whose value for a point M is:

$$p(M) = \frac{(d(M))^2}{2}$$

The minimization process uses the force field $\mathbf{f}_p$ derived from the potential field p, which is in this case:

$$\mathbf{f}_p(M) = -d(M)\boldsymbol{\nabla}\left(d(M)\right)$$

where $\boldsymbol{\nabla}$ is the gradient operator. A good approximation of this last form is simply the vector $\overrightarrow{MP}$[2].

This vector $\overrightarrow{MP}$ can be computed by an euclidean distance transform which needs only a few passes on the image [12]: it requires the storage of a complete vector (three coordinates in 3D) per point. However, as we manipulate a big amount of data, we prefer to use chamfer's distance (see [6]) which is only an estimation of the distance but gives one single value per point. An other efficient solution is to use a hierarchical data structure, like octrees [21].

Now, the potential energy of the *object* Obj is:

$$E_p = \int_{P \in Obj} p(P) dP$$

The problem is to find a 3D rigid transformation of the *object* which minimize this energy.

For that purpose, one can use classical numerical minimization algorithms (see [4, 7, 9, 19, 31] for example).

Because of the potential, it seems to us more natural to use a mechanical approach. In fact, a direct application of the fundamental laws of the dynamic avoids the extensive analytical computation of the potential derivatives with respect to the transformation parameters.

[2] If all points in a neighborhood of M have the same closest *model* point P, there is an equality between both formulations.

2.3 Minimization algorithm

The principle is the potential minimization using mechanical elements is the following. We consider the *object* as a solid (a system of mass points where the distances between all pairs of points remain constant) by attributing the elementary mass of the voxel to its center of mass. By assuming that we know the voxel dimensions, we solve the scaling problem. Deriving from the potential field, there is a force field which will draw the *object* towards a potential minimum. The whole forces which apply to the *object* may be represented by a force torque $\{\mathcal{T}_{\mathbf{f}}\}$. According to the general theorem of the dynamic, this force torque is equal to the dynamic torque of the *object*. By integration with respect to time, we obtain the behavior of the transformation parameters with:

$$\left\{ \begin{array}{rcl} \dot{\mathbf{t}} & = & \mathbf{v}(G) \\ \dot{\mathbf{r}} & = & \mathbf{J}^{-1}(G)\boldsymbol{\sigma}(G) \end{array} \right. \quad \text{and} \quad \left\{ \begin{array}{rcl} \ddot{\mathbf{t}} & = & \dfrac{\mathcal{R}_{\mathbf{f}}}{m(Obj)} \\ \ddot{\mathbf{r}} & = & \mathbf{J}^{-1}(G)\mathcal{M}_{\mathbf{f}}(G) \end{array} \right.$$

where $\mathbf{t}$ is the translation vector, $\mathbf{r}$ the rotation vector (both give the complete transformation), $\mathbf{v}(G)$ the velocity of the center of mass G of the *object*, $\mathbf{J}(G)$ the inertia matrix computed with respect to G, $\boldsymbol{\sigma}(G)$ the angular momentum of the *object* with respect to G and $\mathcal{R}_{\mathbf{f}}$ and $\mathcal{M}_{\mathbf{f}}(G)$ are the components of the force torque.

For more details, these mechanical theory elements are presented in appendix A and the link with the transformation parameters in appendix B.

We are then able to compute the motion of any solid subject to a potential field.

However, this single relation generates a system which does not reach stability, i.e. a minimum of potential. In fact, the global energy[3] is constant and the system cannot stop. By analogy, the motion looks like the one of a non damped pendulum. We will introduce "damping" for our system. The characteristic of "damping" is the following: it dissipates energy, so the global energy decreases.

A first refined solution is to introduce viscosity, then any solid subject to the potential field stop by itself at the potential minimum.

At each point P of the *object* we apply a viscosity force $\mathbf{f}_v(P) = -k_v\mathbf{v}(P)$ where k_v is the viscosity constant and $\mathbf{v}(P)$ the velocity of the point P. It comes to deal with a global force $\mathbf{f}$ equal to the sum of the force $\mathbf{f}_p$ deriving from the potential field and of the viscosity force $\mathbf{f}_v$. the force torque $\{\mathcal{T}_{\mathbf{f}}\}$ is then equal to $\{\mathcal{T}_{\mathbf{f}_p}\} + \{\mathcal{T}_{\mathbf{f}_v}\}$ where $\{\mathcal{T}_{\mathbf{f}_v}\}$ is the viscosity

[3]The global energy E is equal to the sum of the potential energy E_p and of the kinetic energy E_k. We have $E_k = \frac{1}{2}\left(m(Obj)\mathbf{v}^2(G) + \boldsymbol{\omega}.\mathbf{J}\boldsymbol{\omega}\right)$, see appendix A for notations.

force torque. We have:

$$\{\mathcal{T}_{\mathbf{f}_v}\} = \begin{cases} -k_v \mathbf{v}(G) \\ -\dfrac{k_v}{m(Obj)} \boldsymbol{\sigma}(G) \end{cases}$$

which gives a very simple expression of the viscosity force torque which needs no computational effort.

However, we did not retain this solution, because we need first to identify the constant k_v which depends on the studied *object* and second the *object* needs an "infinite" time to reach the minimum (i.e. too many iterations).

We prefer then an other solution. Let E_p be the potential energy of the *object*, we have:

$$E_p = \int_{P \in Obj} v(P)\, dP$$

The potential energy is a part of the global system (equal to the sum of the potential energy and the kinetic energy), and it passes through a minimum when a stability point is reached. We will use this property to find that minimum, when looking at the potential energy during the motion.

We propose the following algorithm.

1. At time t we compute the force torque $\{\mathcal{T}_{\mathbf{f},t}\}$and the potential energy $E_{p,t}$. of the *object*.

2. If the potential energy $E_{p,t}$ is less than the potential energy at time $t - dt$, then we compute the new transformation which applies to the object (see appendix B).

3. If the potential energy $E_{p,t}$ is greater than the potential energy at time $t - dt$, then we take the previous system state (at time $t - dt$).

   (a) If the velocity $\mathbf{v}(G)$ and the kinetic moment $\boldsymbol{\sigma}(G)$ are not null (at time $t - dt$), we set them to zero. It is equivalent to set the kinetic energy to zero, which decreases the global energy.

   (b) If the velocity $\mathbf{v}(G)$ and the kinetic moment $\boldsymbol{\sigma}(G)$ are already null (at time $t - dt$), we change the value of the elementary unity of time dt to $\dfrac{dt}{2}$. We are then looking for smaller displacements.

   (c) We compute then the new transformation by using the force torque at time $t - dt$, $\{\mathcal{T}_{\mathbf{f},t-dt}\}$

By applying this algorithm, we ensure that the whole system energy decreases because we set the kinetic energy to zero each time it passes through a maximum (because the potential energy is then minimum) with respect to the time step we use. When the whole energy is not decreasing, we take a smaller time step in order to look for smaller displacements.

We stop the algorithm when these displacements become too small, that is, when dt becomes too small (for example lower to 0.1 if the initial value of dt was 1).

3 Results

We first present in this section a bench test on a synthetic object, in order to discuss local minima. The main remark we make is that the right match is always found if the rotation angle between images to register is not too large. This conclusion must of course be moderated by the specificity of the test we made.

Then, we will present results on real medical images (same modality or different modalities): two experimental studies with CT scan of the head and of the skull, and two clinical studies with MRI and PET data.

3.1 Synthetic object

In order to evaluate the performance of our algorithm and its behavior with respect to false matches (i.e. local minima of the potential energy), we try to define a bench test.

For that purpose, we use a synthetic object defined by its equation in spherical coordinates (r, θ, ϕ) with $\theta \in [0 \dots 2\pi]$ and $\phi \in [0 \dots \pi]$:

$$r = \begin{cases} 2\left(2\frac{\phi}{\pi}\right)^3 + 2\,\mathrm{e}^{\left(\left(\theta+\frac{\pi}{3}\right)\left[2\pi-\left(\theta+\frac{\pi}{3}\right)\right]-\pi^2\right)^2}\mathrm{e}^{\left(\phi\left(\frac{\pi}{2}-\phi\right)-\frac{\pi^2}{16}\right)^2}\sqrt{2\left(1-2\frac{\phi}{\pi}\right)} & \phi \leq \frac{\pi}{2} \\ 2\,\left(2-2\frac{\phi}{\pi}\right)^3 + 2\theta\left(2\pi-\theta\right)\left(\theta-\pi\right)^2\frac{81}{20\pi^4}\mathrm{e}^{\left((\phi-\pi/2)(\pi-\phi)-\frac{\pi^2}{16}\right)^2}\sqrt{2\left(2\frac{\phi}{\pi}-1\right)} & \phi > \frac{\pi}{2} \end{cases}$$

This object can be seen in figure 1.

Then we define a set of rigid transformations. We have chosen at random eight translation vectors (one per space quadrant) and eight rotation axes (one per space quadrant too) which can be seen in tables 1 and 2. It gives 64 combinations. For each of them, we apply 18 different angles of rotation (from 5 to 90 degrees with a step of 5 degrees). We apply the 8 single translation vectors too (it corresponds to an angle equal to 0). We have then a set of 1160 different rigid transformations.

We define two bench tests: the first with objects of same resolution, the second with objects of different resolutions. In both cases, we apply the whole set of rigid transformations

to one object and evaluate the algorithm by comparing the expected result (the applied rigid transformation defined by the rotation vector $\mathbf{r}$ and translation vector $\mathbf{t}$) to the found one (the transformation given by the algorithm defined by the rotation vector $\mathbf{r}'$ and translation vector $\mathbf{t}'$). The modulus of the rotation vector is the angle of rotation in degrees. We define the final error e with:

$$e = \|\mathbf{r} - \mathbf{r}'\| + \|\mathbf{t} - \mathbf{t}'\|$$

Results are presented in figures 2 and 3. We give a few comments:

1. the high peak near 0 (which designs the right matches found by the algorithm) contains more of 75% of all tests;

2. the matches which are not found by the algorithm always give a large error (greater than 50), there is then no ambiguity to decide whether the transformation found is the right one or not.

In this measure of the final error e, the value due to the translation error has a minor importance compared to the rotation error. Thus, the final error in rotation is the more significant. This result is in fact not surprising because the final error in translation depends only of the respective positions of the two centers of mass.

We examinate more carefully this rotation error with respect to the initial rotation angle. Results are in figures 4 and 5. It appears that the right match is always found when the initial angle is not too big (for instance less than 30 degrees in this example). Then the percentage of successful matches decreases as the initial rotation angle increases.

This limitation seems not to be too restrictive for medical applications. In fact, we always know the position of image axis with respect to the patient for each acquisition (for example, we know that we have sagittal or coronal views of the brain). These positions give us a first estimate of the transformation: before to register a coronal image and a sagittal one, we will transpose one of them in order to obtain two coronal or two sagittal images. The final rotation which still exists between both images has generally a small angle. In order to illustrate this, we always find a good registration for all the real cases we treated as we will see it below. The local minima have exclusively appeared when synthetic data were used.

3.2 CT Scan images with stereotaxic frame

We have two images of the same head coupled with a stereotaxic frame. Images have respectively 135 and 126 slices of 256x256 voxels, with a size of 1x1x1.5 mm^3. Some slices of both images are shown in figure 6. Thanks to the stereotaxic frame, we are able to compute the

right transformation between both images. Then we extract the skull of these images (with a threshold operation) and register both skulls using our algorithm. The difference between both transformations is less than one voxel for the translation and less than one degree for the rotation. We show in figure 7 slices of the first image already shown in figure 6 and the corresponding slices of the second image after resampling.

In order to make the results clearer, we show again the lower left slice of the first image with a frame of little crosses (left in figure 8). As we show the corresponding slice of the second image after resampling with the same frame of little crosses (right in figure 8), it is easy to verify the accuracy of the algorithm. The third image of figure 8 presents the superimposition of edges detected in the slice of the first image on the corresponding slice of the second image after resampling.

The accuracy of the result is perhaps more convincing in figure 9 where coronal views are presented: at the top, from left to right, we present coronal slices of respectively the first original scan image, the second original scan image and the second scan image after resampling (please notice that top and bottom of the third head are truncated because of the difference of size of both original images); at the bottom, from left to right, the same coronal slice of the first image with a frame of little crosses, the corresponding slice of the second image after resampling with the same frame of little crosses and superimposition of edges of the first image on the second one after resampling. This shows clearly the three-dimensional nature of the registration.

3.3 Skulls

We have two images of the same skull in two different positions (see figure 10). The size of the voxel is 1.0x1.0x0.8 mm^3 and one of both image (on the right) is truncated with respect to the other. Images have a size of 220x128x161. Both skull images are easily transformed into binary images by thresholding. We present the result of the registration in figure 11: on the right, four slices of the first original data superimposed with a frame of little crosses; on the left, the four corresponding slices of the second image after resampling with the found transformation superimposed with the same frame. This frame helps to evaluate visually the accuracy of the match.

Coronal views of the skull are presented in figure 12: at the top right a coronal slice of the first original data, and left a coronal slice of the second original data; at the bottom, the same coronal slice of the first image with a frame of little crosses, the corresponding slice of the second image after resampling with the same frame of little crosses.

3D representations of the skulls are presented in figure 13 (one skull is shifted with respect

to the other for clarity). The same 3D representations after registration can be viewed in figure 14: little crosses present typical correspondences.

3.4 MRI images of the brain

We have two MRI images of the same patient head, taken at different dates. They have respectively 54 and 51 slices of 256x256 voxels. The voxel size is 0.94x0.94x3 mm^3. Some slices of the original images can be seen in figures 15 and 16. We can easily extract the brain from both images by using mathematical morphology (see [23]). We compute the registration with both brains and apply the found transformation in order to resample one of the images. We show in figure 17 some slices of the second image after resampling, corresponding to the slices of figure 15.

Now if we look carefully at the central slice of each figure 15, 16 and 17, we can see in the first original brain a thin black structure (the middle cerebral artery) which does not appear completely in the corresponding slice of the second original data. If one look at the corresponding slice of the resampled image, one can see now this whole artery.

This central slice can be seen in figure 18 too: from left to right, the central slice of figure 15 of the first image, the corresponding slice of the second image after resampling (both of them are presented with little crosses pointing out some details) and the superimposition of edges extracted from the first image on the second image.

To be more convincing, we present sagittal and coronal slices of the two original images and of the resampled one in figures 19 and 20: at the top from left to right, a slice of the first original data, a slice of the second original data and the slice of the second image after the registration; at the bottom from left to right, the same slice of the first image with little crosses pointing out some details, the corresponding slice of the second image after resampling with the same little crosses and the superimposition of edges extracted from the first image on the second image. These figures seem blurred because we resampled them a second time along the vertical axis in order to obtain quasi-isotropic voxels, for display purpose only.

3.5 Brain: PET-IRM registration

We have an MRI image of size 256x256x120 of the brain with voxels of size 1.3x1.3x1.3 mm^3 and no inter-slice distance (acquired on a GE Signa-Advantage 1.5 T), we show some slices of this image in figure 21. We have extracted the brain with an automatic algorithm, using mathematical morphology operators [17, 23].

We have also a PET image of size 256x256x7 of the same brain with voxels of size 1x1x9 mm^3 and an inter-slice distance of 3 mm (acquired on a TTV03), we show the seven slices of this image in figure 22. We can extract the brain by thresholding.

In figure 23, one can see the trace of PET slices on slices of MRI brain after automatic registration of both images. Please notice the typical orientation of the PET slices with respect to the sagittal view of the brain.

The registration takes 134 seconds CPU on a DEC 5000 workstation. In figure 24, we have resampled the MRI slices corresponding to PET slices. We have extracted the edges of these resampled slices with a classical algorithm [29] and superimposed them with original PET slices in figure 25. This shows the accuracy of the registration.

The good results already obtained should allow clinical studies in Neurology, such as the follow up of diseases, or the localization of various brain functions.

4 Conclusion

We presented a new matching algorithm between 3D objects which does not need explicit markers. The principle of our method is a minimization of a potential which is solved by using an application of the fundamental laws of dynamics. The algorithm, in its actual form, allows us to register either mono-modality or multi-modalities images.

We reported an experiment with a synthetic object, which allowed us to study the algorithm behavior with respect to local minima. The main conclusion was the good registration, i.e. the global minimum, is always found when the rotation angle is not too big, which is always the case for medical images according that one knows the geometry of the acquisition.

Another solution towards this limitation is to try several initial positions for both objects to register (see [4, 7]), the trouble is then the computational cost of each trial. Then we plan to develop our algorithm in order to be able to do multiscale registration and to reduce this computational cost.

Acknowledgment

This work was partially supported by Digital Equipment Corporation. We thank Dr. Jael Travere (Cyceron center, CEA, Caen, France), Dr. R. Kikinis (Department of Radiology, Brigham and Women's Hospital, Harvard Medical School, Boston, MA, USA) and GE-CGR (Buc, France) for providing medical data. Dr. Nicholas Ayache and Dr. Jean-Philippe Thirion gave a substantial help in the redaction of this paper.

A Mechanical Theory Elements

In the following, we assume that we are in a euclidean and galilean reference frame. We recall now a few basic definitions (inertia parameters, kinetic, dynamic and force torques) and present some relations between them. We will then be able to deduce the parameters of the transformation of the *object* derived from the motion due to the potential field (see [5]).

A.1 Notations and definitions

We denote by $\mathbf{v}(P)$ the velocity of a point P $\boldsymbol{\gamma}(P)$ its acceleration which can be computed from:

$$\begin{aligned} \mathbf{v}(P) &= \dot{P} \\ \boldsymbol{\gamma}(P) &= \ddot{P} \end{aligned}$$

where dot means the derivation of the point coordinates with respect to time.

The torque of a vector field $\mathbf{f}$ for a solid Obj are the resultant vector $\mathcal{R}_{\mathbf{f}}$ and the moment vector with respect to a point Q, $\mathcal{M}_{\mathbf{f}}(Q)$. The torque is denoted by $\{\mathcal{T}_{\mathbf{f}}\}$ and can be computed with:

$$\{\mathcal{T}_{\mathbf{f}}\} = \left\{ \begin{array}{lcl} \mathcal{R}_{\mathbf{f}} & = & \displaystyle\int_{P \in Obj} \mathbf{f}(P)\, dP \\ \mathcal{M}_{\mathbf{f}}(Q) & = & \displaystyle\int_{P \in Obj} \overrightarrow{QP} \times \mathbf{f}(P)\, dP \end{array} \right.$$

where $\mathbf{f}(P)$ denotes the value of the vector field $\mathbf{f}$ at P, and $\times$ the vector product.

Once the moment vector $\mathcal{M}_{\mathbf{f}}(Q)$ is computed with respect to a point Q, it can be easily computed with respect to any point R by:

$$\mathcal{M}_{\mathbf{f}}(R) = \mathcal{M}_{\mathbf{f}}(Q) + \overrightarrow{RQ} \times \mathcal{R}_{\mathbf{f}}$$

A.2 Inertia Parameters

The inertia parameters of a solid Obj are useful for a simplified description of its motion: they are the center of mass and the inertia matrix.

Let us call G the center of mass of the *object* which can be computed with:

$$\int_{P \in Obj} P\, dm(P) = m(Obj)\, G$$

where $m(Obj)$ is the whole mass of the *object* and $dm(P)$ is the elementary mass associated to any point $P \in Obj$ [4]. We set $dm(P) = 1$ in our experiments.

[4] We have obviously $\displaystyle\int_{P \in Obj} dm(P) = m(Obj)$.

Let us denote $\mathbf{J}(Q)$ the inertia matrix of the *object* computed with respect to a point $Q \in Obj$ (computed in an orthonormal basis (X, Y, Z)).

$$\mathbf{J}(Q) = \begin{bmatrix} \int_{P \in Obj} (y^2 + z^2)\, dm(P) & -\int_{P \in Obj} xy\, dm(P) & -\int_{P \in Obj} zx\, dm(P) \\ -\int_{P \in Obj} xy\, dm(P) & \int_{P \in Obj} (z^2 + x^2)\, dm(P) & -\int_{P \in Obj} yz\, dm(P) \\ -\int_{P \in Obj} zx\, dm(P) & -\int_{P \in Obj} yz\, dm(P) & \int_{P \in Obj} (x^2 + y^2)\, dm(P) \end{bmatrix}$$

where (x, y, z) are the coordinates of the vector $\overrightarrow{QP}$ in (X, Y, Z).

The eigenvectors of this matrix give the principal axes of the solid Obj and the eigenvalues are the inertia momentums with respect to these axes.

According to the generalized Huyghens theorem, we can compute the inertia matrix with respect to any point of the *object* and in particular to G, thanks to:

$$\mathbf{J}(Q) = \mathbf{J}(G) + \mathbf{J}(Q, \{G, m(Obj)\})$$

where $\mathbf{J}(Q, \{G, m(Obj)\})$ is the inertia matrix with respect to the point Q of the point G with a mass $m(Obj)$.

Finally, let $\mathbf{J}'(Q)$ be the inertia matrix of the *object* with respect to the point Q in an orthonormal basis (X', Y', Z') and let $\mathbf{M}$ be the transformation matrix from basis (X, Y, Z) to basis (X', Y', Z'), then:

$$\mathbf{J}'(Q) = \mathbf{M}\, \mathbf{J}(Q)\, \mathbf{M}^{-1}$$

A.3 Kinetic Torque

The velocity vector field of the solid Obj is described by the kinetic torque, denoted by $\{\mathcal{T}_{\mathbf{v}}(Obj)\}$, whose elements are given with respect to an arbitrary point Q:

$$\{\mathcal{T}_{\mathbf{v}}(Obj)\} = \begin{cases} \mathcal{R}_{\mathbf{v}} & = \int_{P \in Obj} \mathbf{v}(P)\, dm(P) \\ \mathcal{M}_{\mathbf{v}}(Q) & = \int_{P \in Obj} \overrightarrow{QP} \times \mathbf{v}(P)\, dm(P) \end{cases}$$

The torque moment of the velocity field at Q is called the kinetic moment (or angular momentum) in Q and is usually denoted by $\boldsymbol{\sigma}(Q)$. Its expression simplifies when it is expressed with respect to the center of mass G. Let us denote by $\boldsymbol{\omega}$ the angular velocity vector of the solid Obj. The kinetic torque with respect to G is then:

$$\{\mathcal{T}_{\mathbf{v}}(Obj)\} = \begin{cases} m(Obj)\, \mathbf{v}(G) \\ \mathbf{J}(G)\, \boldsymbol{\omega} \end{cases}$$

A.4 Dynamic Torque

The acceleration vector field of the solid Obj is described by the dynamic torque, denoted by $\{\mathcal{T}_{\boldsymbol{\gamma}}(Obj)\}$, whose elements are given with respect to an arbitrary point Q:

$$\{\mathcal{T}_{\boldsymbol{\gamma}}(Obj)\} = \left\{ \begin{array}{lcl} \mathcal{R}_{\boldsymbol{\gamma}} & = & \displaystyle\int_{P \in Obj} \boldsymbol{\gamma}(P)\, dm(P) \\ \mathcal{M}_{\boldsymbol{\gamma}}(Q) & = & \displaystyle\int_{P \in Obj} \overrightarrow{QP} \times \boldsymbol{\gamma}(P)\, dm(P) \end{array} \right.$$

The torque moment of the acceleration field at Q is called the dynamic moment of Q and is usually denoted by $\boldsymbol{\delta}(Q)$. In general, the derivative with respect to the time of the kinetic moment $\boldsymbol{\sigma}$ is not equal to the dynamic moment $\boldsymbol{\delta}$. But, when these moments are expressed with respect to the center of mass G, this equality holds and we obtain:

$$\{\mathcal{T}_{\boldsymbol{\gamma}}(Obj)\} = \left\{ \begin{array}{lcl} m(Obj)\, \boldsymbol{\gamma}(G) & = & m(Obj)\, \dot{\mathbf{v}}(G) \\ \dot{\boldsymbol{\sigma}}(G) & = & \mathbf{J}(G)\, \dot{\boldsymbol{\omega}} \end{array} \right.$$

A.5 Force Torque

The solid Obj is subject to a potential field p. From this potential field derives a force field $\mathbf{f}_p$ which causes the motion of the solid Obj towards a minimum of potential energy. This force field is:

$$\mathbf{f}_p(M) = -\boldsymbol{\nabla}\left(p(M)\right)$$

where $\boldsymbol{\nabla}$ is the gradient operator. According that the potential field has the form presented in section 2.2, i.e. $p(M) = \dfrac{(d(M))^2}{2}$, then the expression of the force field becomes:

$$\mathbf{f}_p(M) = -d(M)\boldsymbol{\nabla}\left(d(M)\right)$$

Let us denote by $\mathbf{f}(P)$ the sum of all forces which apply at point P. It includes obviously the force $\mathbf{f}_p$ deriving from the potential field but can include another forces (like viscosity forces).

The forces of the force field $\mathbf{f}$ which apply to the solid Obj can be described by the force torque denoted by $\{\mathcal{T}_{\mathbf{f}}\}$ whose reduction elements in a point Q are the resultant vector $\mathcal{R}_{\mathbf{f}}$ and the moment vector with respect to Q, $\mathcal{M}_{\mathbf{f}}(Q)$:

$$\{\mathcal{T}_{\mathbf{f}}\} = \left\{ \begin{array}{lcl} \mathcal{R}_{\mathbf{f}} & = & \displaystyle\int_{P \in Obj} \mathbf{f}(P)\, dP \\ \mathcal{M}_{\mathbf{f}}(Q) & = & \displaystyle\int_{P \in Obj} \overrightarrow{QP} \times \mathbf{f}(P)\, dP \end{array} \right.$$

We choose to compute the potential for the whole space with a distance transform, to store it, and then we calculate forces only where we need it. There exists an alternative which is to compute the force field for the whole space with the euclidean distance transform [12] and to store it. This second approach comes to store one entire vector per each space point which is more expensive in term of memory.

According to the general theorem of the dynamic, we know that the force torque $\{\mathcal{T}_{\mathbf{f}}\}$ is equal to the dynamic torque of the *object* Obj, $\{\mathcal{T}_{\boldsymbol{\gamma}}(Obj)\}$.

As we have expressed the dynamic torque with respect to the center of mass G, we have to express the force moment with respect to G too. It comes:

$$\mathcal{M}_{\mathbf{f}}(G) = \mathcal{M}_{\mathbf{f}}(Q) - \overrightarrow{QG} \times \mathcal{R}_{\mathbf{f}}$$

B Transformation parameters

Because of the force field which derives from the potential generated by the *model*, the solid Obj subject to it will exhibit motion parameterized by time. We describe it by a series of successive positions, with an elementary unity of time dt between two successive positions.

Let us denote the transformation parameters from the initial position (at time 0) to the position at time t by the rotation vector $\mathbf{r}_t$ and the translation vector $\mathbf{t}_t$. Of course, we have $\mathbf{r}_0 = \mathbf{t}_0 = \vec{0}$.

We express this transformation with respect to the center of mass G. It allows us to apply rotation and translation in any order. The derivative with respect to time of the rotation vector $\mathbf{r}$ and the translation vector are respectively the angular velocity vector $\boldsymbol{\omega}$ (by definition of the angular velocity vector) and the velocity of G, $\mathbf{v}(G)$ (because the translation between two positions is defined by the two positions of the point G). We have then:

$$\begin{cases} \dot{\mathbf{t}} &= \mathbf{v}(G) \\ \dot{\mathbf{r}} &= \boldsymbol{\omega} &= \mathbf{J}^{-1}(G)\boldsymbol{\sigma}(G) \end{cases}$$

According to the general theorem of the dynamic , the derivative of the kinetic torque with respect to time expresses simply with the force torque. We obtain for the second derivative of the transformation parameters with respect to time:

$$\begin{cases} \ddot{\mathbf{t}} &= \dot{\mathbf{v}}(G) &= \dfrac{\mathcal{R}_{\mathbf{f}}}{m(Obj)} \\ \ddot{\mathbf{r}} &= \mathbf{J}^{-1}(G)\dot{\boldsymbol{\sigma}}(G) &= \mathbf{J}^{-1}(G)\mathcal{M}_{\mathbf{f}}(G) \end{cases}$$

We are then able to compute the transformation parameters from the initial position to the position at time $t + dt$ (i.e. $\mathbf{r}_{t+dt}$ and $\mathbf{t}_{t+dt}$).

At time t, we are able to compute the force torque which applies to the *object*, i.e. $\mathcal{T}_{\mathbf{f},t} = \{\mathcal{R}_{\mathbf{f},t}, \mathcal{M}_{\mathbf{f},t}(G)\}$. According to the general theorem of the dynamic, this force torque is equal to the dynamic torque, we are then able to link it to the kinetic torque. We obtain:

$$\begin{aligned} \mathbf{v}_{t+dt}(G) &= \mathbf{v}_t(G) + \frac{\mathcal{R}_{\mathbf{f},t}}{m(Obj)}\, dt \\ \boldsymbol{\sigma}_{t+dt}(G) &= \boldsymbol{\sigma}_t(G) + \mathcal{M}_{\mathbf{f},t}(G)\, dt \end{aligned}$$

where G_t is the center of mass at time t. We consider the solid Obj without motion at time 0: $\mathbf{v}_0(G) = \boldsymbol{\sigma}_0(G) = \vec{0}$.

This kinetic torque gives us the new transformation parameters at time $t + dt$:

$$\begin{aligned} \mathbf{t}_{t+dt} &= \mathbf{t}_t + \mathbf{v}_{t+dt}(G)\, dt \\ \mathbf{r}_{t+dt} &= \mathbf{r}_t + \mathbf{J}_t^{-1}(G)\, \boldsymbol{\sigma}_{t+dt}(G)\, dt \end{aligned}$$

where $\mathbf{J}_t(G)$ is the inertia matrix of the *object* with respect to G at time t. Let $\mathbf{R}$ be the rotation matrix due to the vector $\mathbf{r}$, we have then (because $\mathbf{R}^{-1} = \mathbf{R}^T$):

$$\mathbf{J}_t^{-1}(G) = \mathbf{R}_t\, \mathbf{J}_0^{-1}(G)\, \mathbf{R}_t^T \ .$$

References

[1] N.M. Alpert, J.F. Bradshaw, D. Kennedy, and J.A. Correia. The principal axes transformation - a method for image registration. *The journal of nuclear medicine*, 31(10), October 1990.

[2] N. Ayache. *Artificial vision for mobile robots: stereo vision and multisensory perception.* MIT Press, 1991.

[3] R. Bajcsy and S. Kovačič. Multiresolution elastic matching. *Computer Vision, Graphics, and Image Processing*, 46:1–21, 1989.

[4] P.J. Besl and McKay N.D. A method for registration of 3d shapes. *IEEE Transactions on PAMI*, 14:239–256, February 1992.

[5] J.C. Bône. *Mécanique générale.* Ecole centrale des arts et manufactures, 1986. Paris.

[6] G. Borgefors. Distance transformations in arbitrary dimensions. *Computer Vision, Graphics, and Image Processing*, 27:321–345, 1984.

[7] G. Borgefors. Hierarchical chamfer matching: A parametric edge matching algorithm. *IEEE Transactions on PAMI*, 10(6):849–865, november 1988.

[8] M.E. Brummer and al. Automatic detection of brain contours in mri data sets. In *XIIth international conference on Information Processing in Medical Imaging (IPMI), Wye, Kent, England*, pages 188–204, July 1991. Lecture notes in Computer Science 511, Heidelberg, Springer Verlag.

[9] L. Brunie, S. Lavallée, and R. Szeliski. Using force fields derived from 3d distance maps for inferring the attitude of a 3d rigid object. In *2nd European Conference on Computer Vision (ECCV 92)*, May 18–23 1992. Santa Margherita, Ligure, Italy.

[10] I. Cohen, L.D. Cohen, and N. Ayache. Using deformable surfaces to segment 3d images and infer differential structures. *Computer Vision, Graphics, and Image Processing: image understanding*, 1992. In press.

[11] D.L. Collins, T.M. Peters, and A.C. Evans. Multiresolution image registration and brain structure segmentation. In *IEEE EMBS satellite symposium on 3D advanced image processing in medicine*, November 2–4 1992. Rennes, France.

[12] P.E. Danielsson. Euclidean distance mapping. *Computer Graphics and Image Processing*, 14:227–248, 1980.

[13] A.C. Evans, C. Beil, S. Marret, C.J. Thompson, and A. Hakim. Anatomical-functional correlation using an adjustable mri-based region of interest atlas with positron emission tomography. *Journal of Cerebral Blood flow Metabolism*, 8:513–529, 1988.

[14] G. Gerig and al. Automating segmentation of dual-echo mr head data. In *XIIth international conference on Information Processing in Medical Imaging (IPMI), Wye, Kent, England*, pages 175–187, July 1991. Lecture notes in Computer Science 511, Heidelberg, Springer Verlag.

[15] W.E.L. Grimson. *Object recognition by computer: the role of geometric constraints.* MIT Press, 1990.

[16] A. Guéziec and N. Ayache. Smoothing and matching of 3d space curves. In *2nd European Conference on Computer Vision (ECCV 92)*, pages 620–629, May 18–23 1992. Santa Margherita, Ligure, Italy.

[17] K.H. Höhne and W. Hanson. Interactive 3d segmentation of mri and ct volumes using morphological operations. *Journal of Computer Assisted Tomography*, 16(2):285–294, March/April 1992.

[18] D.L.G. Hill and al. Registration of mr and ct images for skull base surgery using point-like anatomical features. *The British journal of radiology*, 64(767):1030–1035, November 1991.

[19] H. Jiang, R. Robb, and K. Holton. Visualization in biomedical computing. In *Proceedings of the SPIE*, volume 1808, pages 196–213, 1992.

[20] O. Kübler and G. Gerig. Segmentation and analysis of multidimensional data-sets in medicine. In *3D Imaging in Medicine*, pages 63–81. Springer Verlag, 1990.

[21] S. Lavallée, R. Szeliski, and L. Brunie. Matching 3d smooth surfaces with their 2d projections using 3d distance maps. In *SPIE, Geometric Methods in Computer Vision*, July 25–26 1991. San Diego.

[22] M.N. Maisey, D.J. Hawkes, and A.M. Lukawiecki-Vydelingum. Synergistic imaging. *European journal of nuclear medicine*, 19:1002–1005, 1992.

[23] G. Malandain. *Filtrage, topologie et mise en correspondance d'images médicales multi-dimensionnelles.* PhD thesis, Ecole Centrale de Paris, Septembre 1992.

[24] G. Malandain and J.M. Rocchisani. Registration of 3d medical images using a mechanical based method. In *IEEE EMBS satellite symposium on 3D advanced image processing in medicine*, November 2–4 1992. Rennes, France.

[25] J.F. Mangin, V. Frouin, and B. Bendriem. Nonsupervised 3d registration of pet and mri data using chamfer matching. In *Conference on medical imaging*, october 27–31 1992. Nuclear Science Symposium, Orlando, Florida.

[26] C.C. Meltzer and al. Anatomical localization for pet using mr imaging. *Journal of computer assisted tomography*, 14(3):418–426, 1990.

[27] S. Minoshima, K.L. Berger, K.S. Lee, and M.A. Mintun. An automated method for rotational correction and centering of the three-dimensional functional brain images. *Journal of Nuclear Medicine*, 33:1579–1585, 1992.

[28] O. Monga, S. Benayoun, and O. Faugeras. From partial derivatives of 3d density images to ridges lines. In *IEEE Computer Vision and Pattern Recognition*, pages 354–389, June 15–18 1992. Champaign, Illinois, USA.

[29] O. Monga, R. Deriche, G. Malandain, and J.P Cocquerez. 3d edge detection by recursive filtering and edge tracking. In *International Conference on Pattern Recognition (ICPR)*, June 1990. Atlantic City, USA.

[30] C.A. Pelizzari and al. Accurate three-dimensional registration of ct, pet and/or mr images of the brain. *Journal of computer assisted tomography*, 13(1):20–26, 1989.

[31] W.H. Press, B.P. Flannery, S.A. Teukolsky, and W.T. Vetterling. *Numerical Recipes in C.* Cambridge University Press, 1988.

[32] S.P. Raya. Low-level segmentation of 3d magnetic resonance brain images - a rule based system. *IEEE Transactions on Medical Imaging*, 12(3):327–337, 1990.

[33] J-P Thirion, O. Monga, S. Benayoun, A. Gueziec, and N. Ayache. Automatic registration of 3d images using surface curvature. In *IEEE Int. Symp. on Optical Applied Science and Engineering*, San-Diego, July 1992.

[34] R.P. Woods, S.R. Cherry, and J.C. Mazziotta. Rapid automated algorithm for aligning and resclicing pet images. *Journal of Computed Assisted Tomography*, 16(1):1–14, 1992.

[35] J. Zhang and al. Multimodality imaging of brain structures for stereotactic surgery. *Radiology*, 175(2):435–441, May 1990.

[36] G. Zubal and al. 3d registration of intermodality medical images. In *Annual international conference of the IEEE engineering in medicine and biology society*, 1991. vol. 13, no 1.

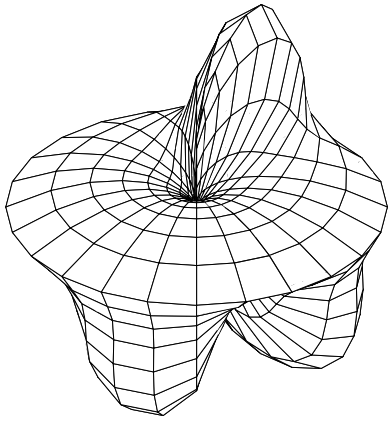

Figure 1: View of the synthetic object.

	$\mathbf{t}_1$	$\mathbf{t}_2$	$\mathbf{t}_3$	$\mathbf{t}_4$	$\mathbf{t}_5$	$\mathbf{t}_6$	$\mathbf{t}_7$	$\mathbf{t}_8$
x	50	-26	14	-37	8	-9	22	-44
y	30	46	-14	-3	30	48	-45	-15
z	47	26	12	37	-24	-45	-16	-16

Table 1: The eight translation vectors chosen at random.

	$\mathbf{r}_1$	$\mathbf{r}_2$	$\mathbf{r}_3$	$\mathbf{r}_4$	$\mathbf{r}_5$	$\mathbf{r}_6$	$\mathbf{r}_7$	$\mathbf{r}_8$
x	8	-14	8	-18	13	-17	4	-17
y	11	17	-7	-11	6	12	-2	-13
z	4	6	12	20	-6	-15	-16	-9

Table 2: The eight rotation axes chosen at random.

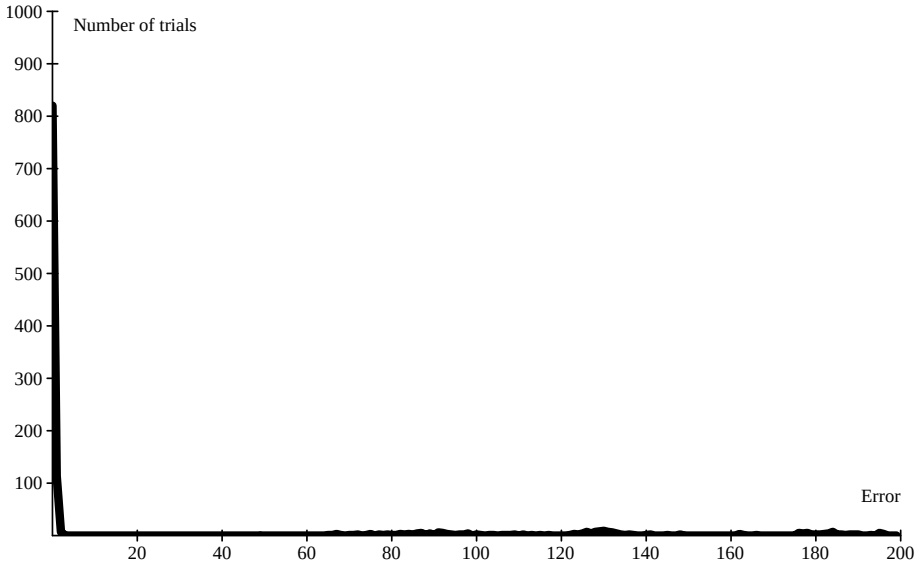

Figure 2: Histogram of errors (for the test with objects of same resolution). Horizontal axis: measure of the final error e; vertical axis: corresponding number of trials.

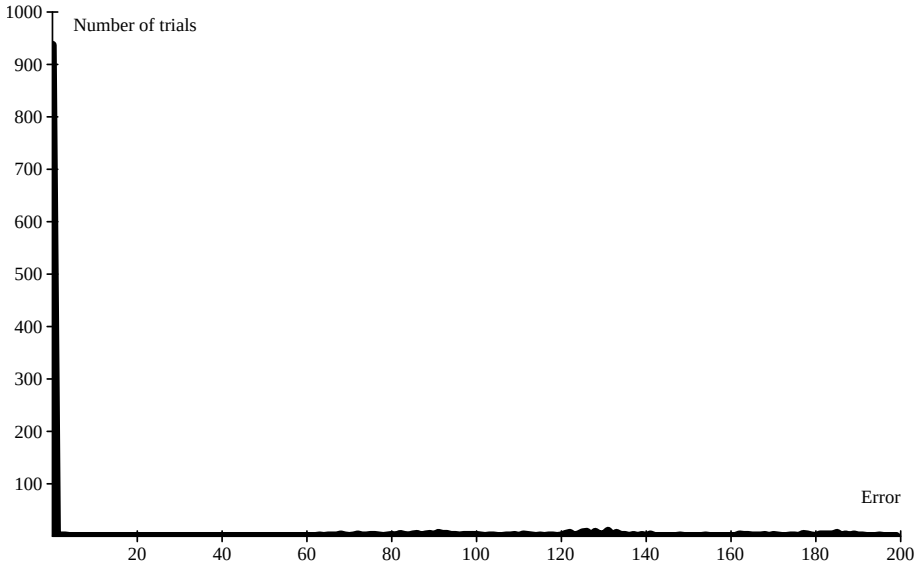

Figure 3: Histogram of errors (for the test with objects of different resolution). Horizontal axis: measure of the final error e; vertical axis: corresponding number of trials.

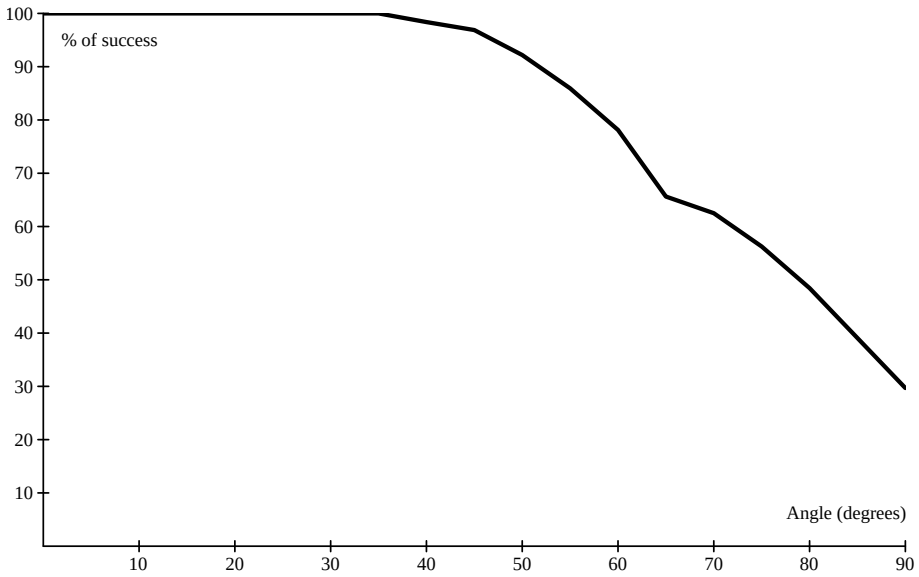

Figure 4: Percentage of right matches with respect to the initial angle of rotation. *Model* and *object* have the same resolution.

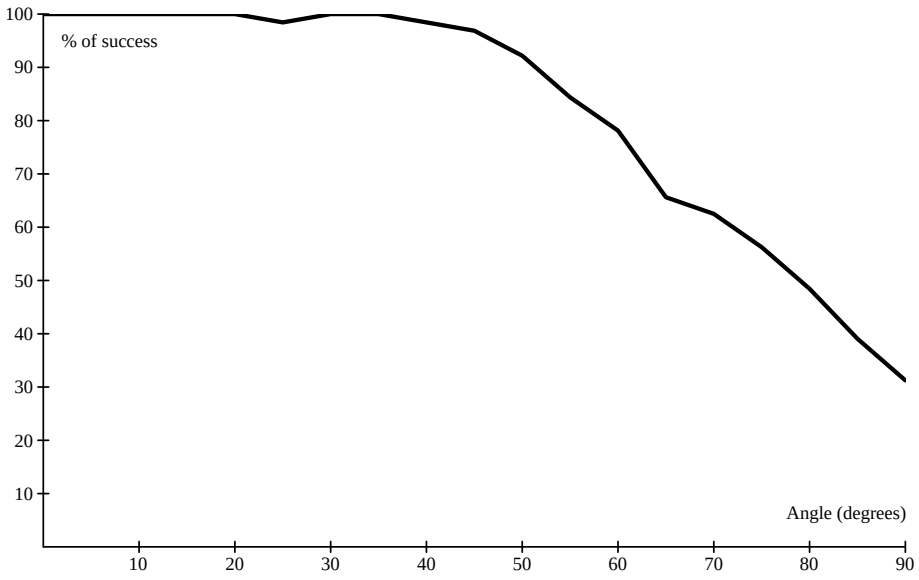

Figure 5: Percentage of right matches with respect to the initial angle of rotation. *Model* and *object* do not have the same resolution.

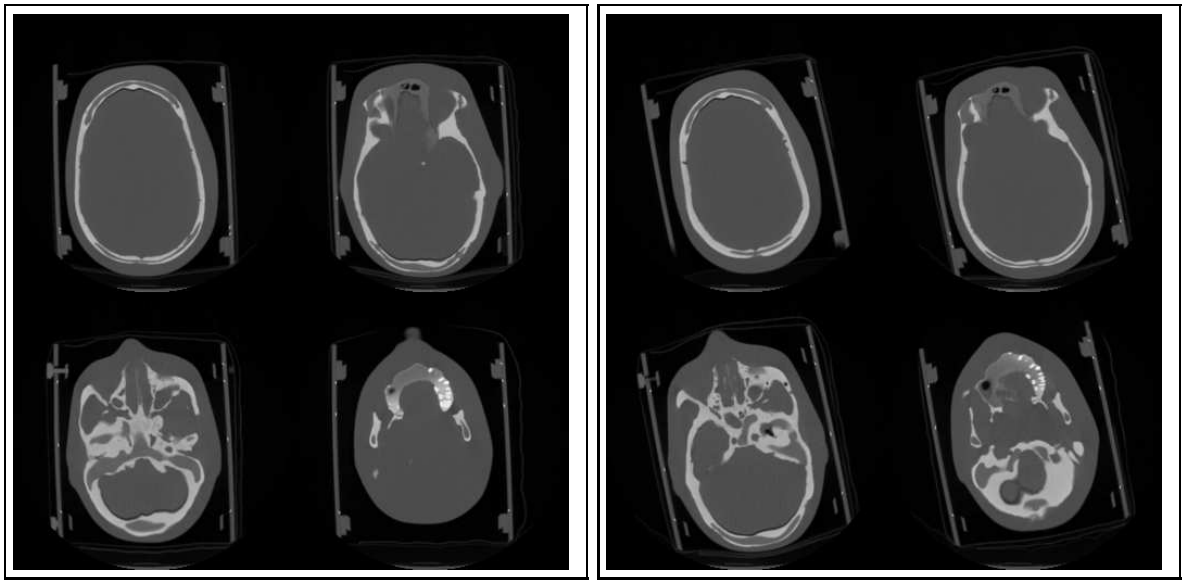

Figure 6: Left and right, four slices of both original data (provided by GE-CGR (Buc, France)). We try to show corresponding slices.

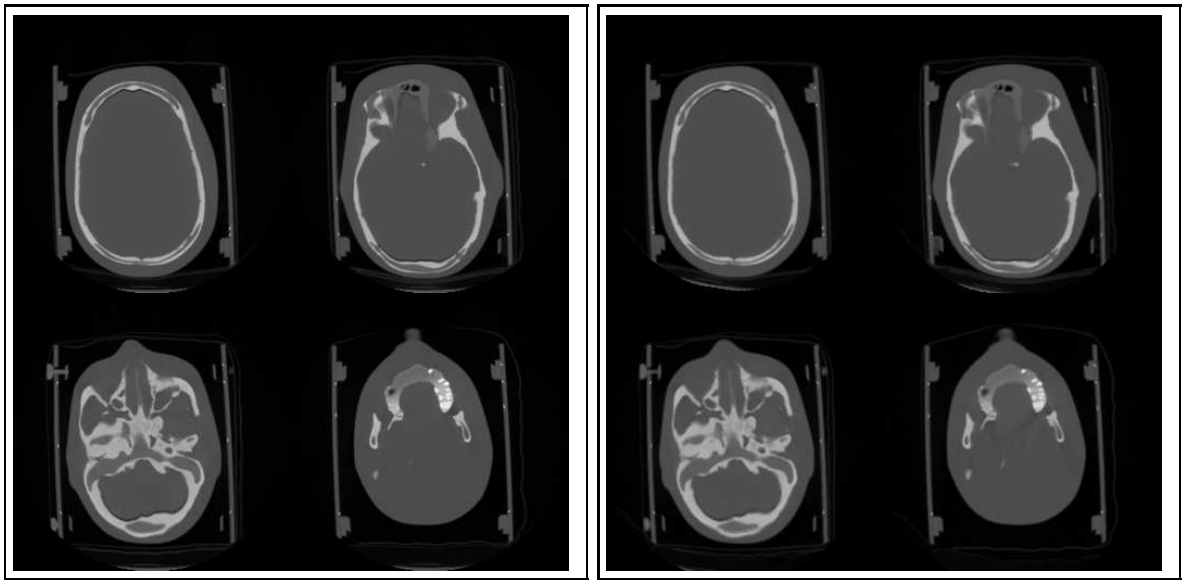

Figure 7: Left, four slices of the first original image. Right, the four corresponding slices of the second image after resampling with the found rigid transformation.

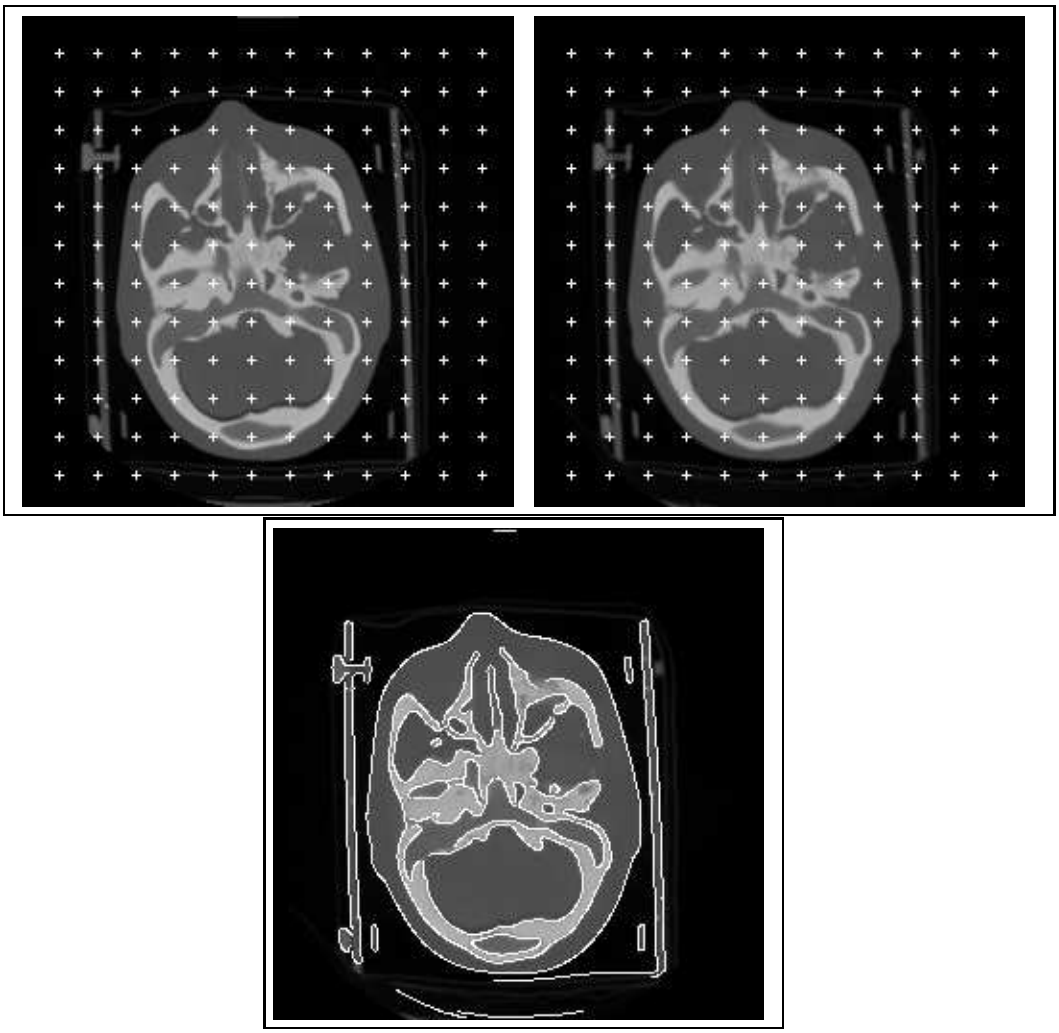

Figure 8: Top, corresponding slices of both images after registration: a frame of little crosses has been overlaid to highlight the accuracy of the result. Bottom, superimposition of the edges of the first image on the second image after resampling.

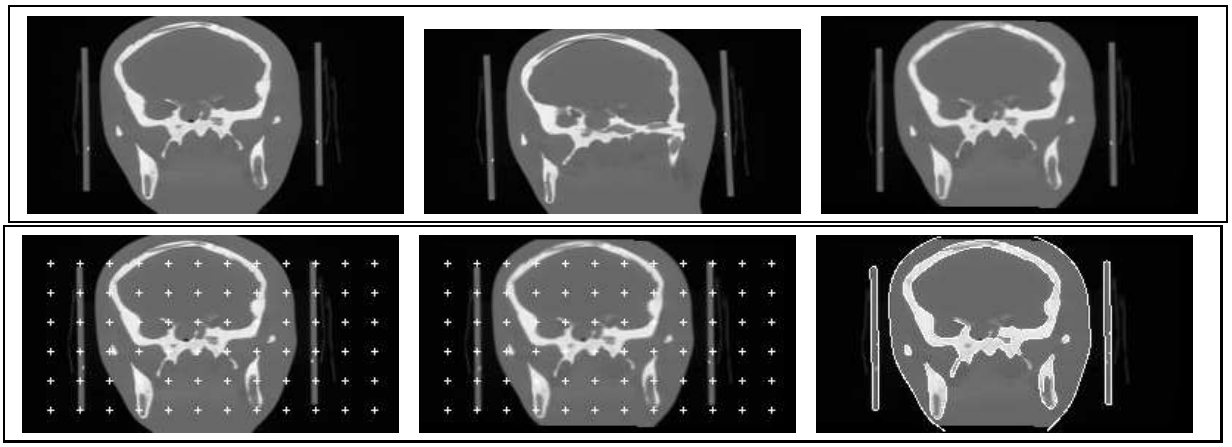

Figure 9: Top, from left to right, we present coronal slices of respectively the first original scan image, the second original scan image and the second scan image after resampling. Bottom, we present corresponding slices after registration with a frame of little crosses and superimposition of the edges of the first image on the second image after resampling.

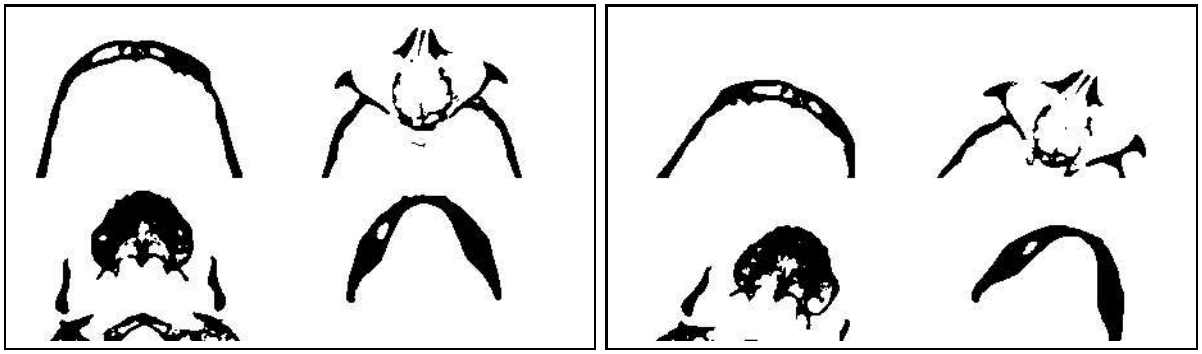

Figure 10: Left and right, four of the 161 slices of both original images. These data are provided by GE-CGR (Buc, France).

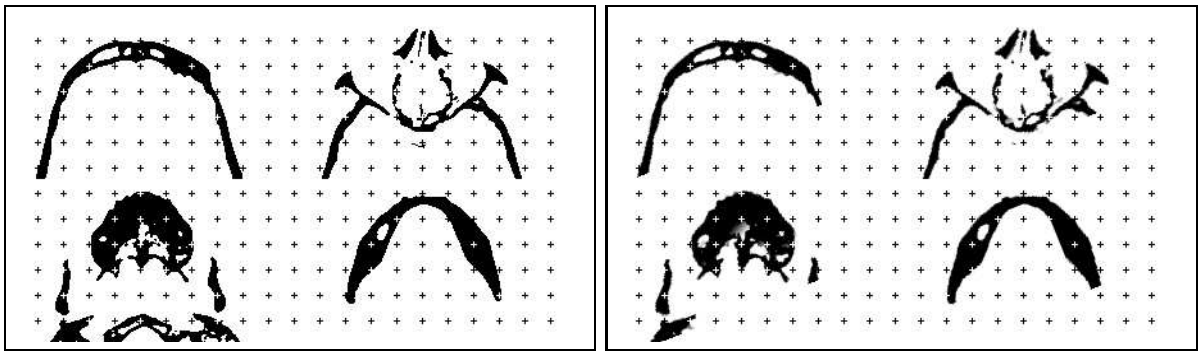

Figure 11: Left, four slices of the first image with a frame of little crosses. Right, the four corresponding slices of the second image after registration with the same frame of little crosses.

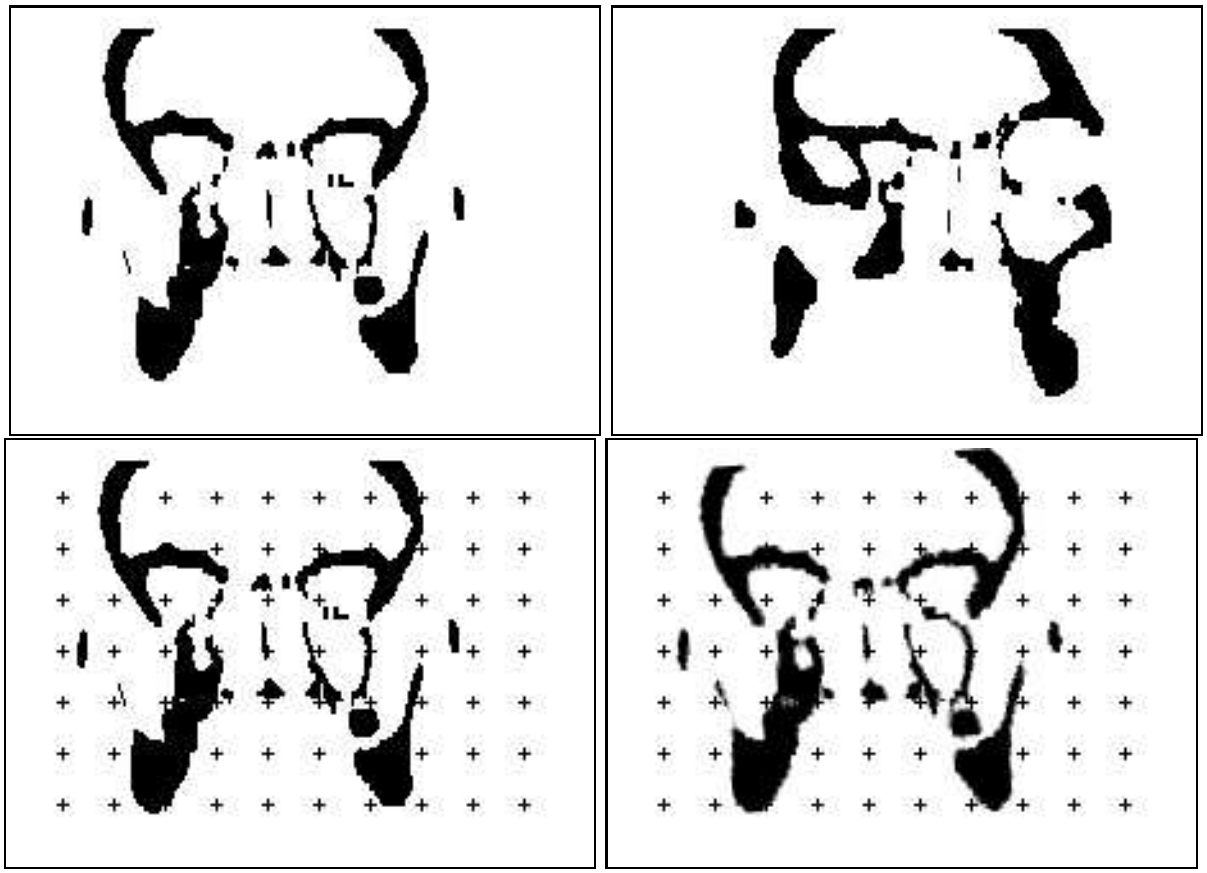

Figure 12: Top, from left to right, coronal slices of respectively the first original scan image and the second original scan image. Bottom, corresponding slices after registration with a frame of little crosses.

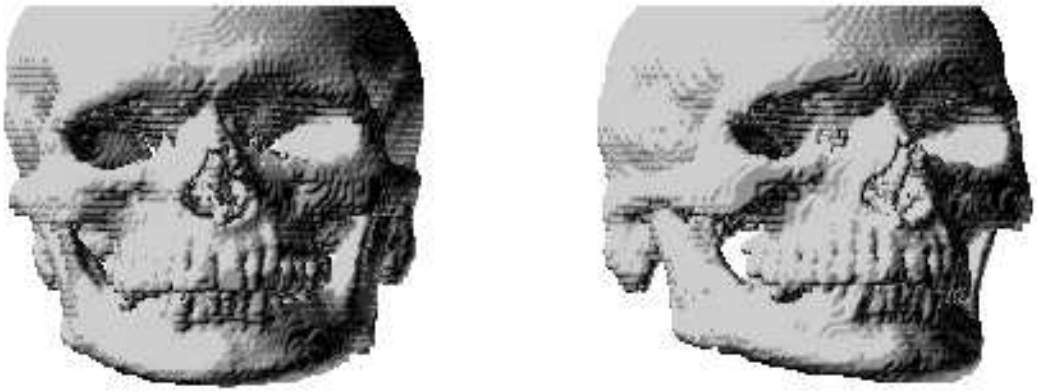

Figure 13: 3D views of both skulls in original position.

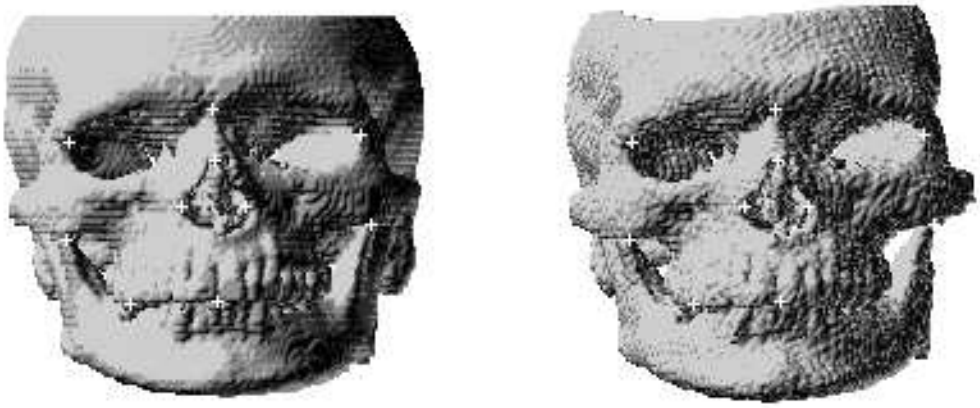

Figure 14: 3D views of both skulls after matching. The upper border of the right skull is no more horizontal because the rotation vector is not vertical. Little crosses are showing the same details in both images.

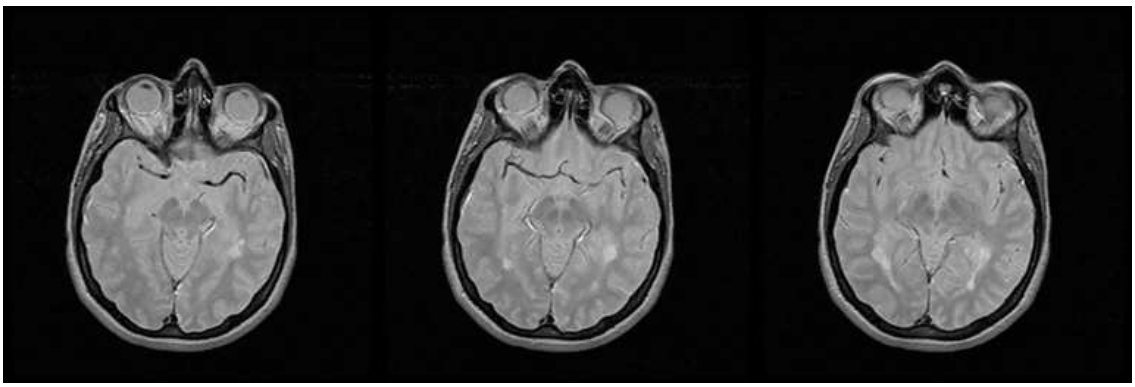

Figure 15: Three consecutive slices of a MRI image of a brain. Please notice the horizontal thin black structure (the middle cerebral artery) at the top of the brain in the central slice. Data are provided by Ron Kikinis, M.D., Department of Radiology, Brigham and Women's Hospital, Harvard Medical School, Boston, MA.

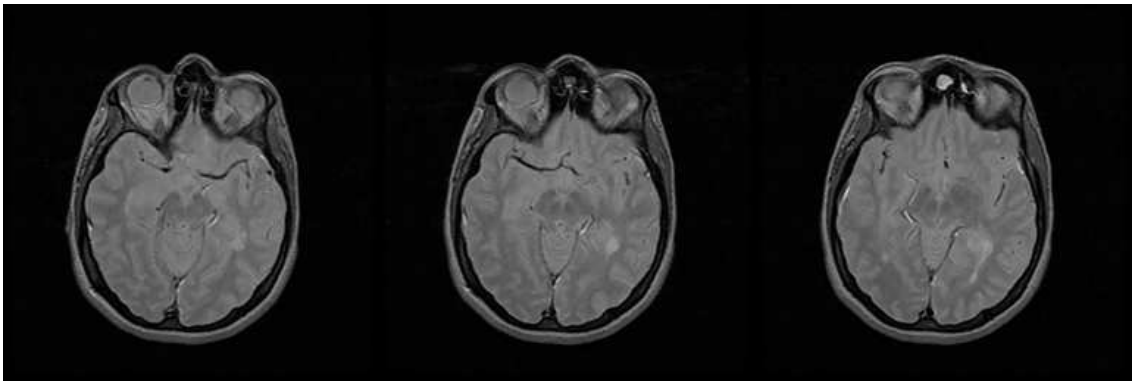

Figure 16: Three consecutive slices of a second MRI study of the same brain two months later. We try to show the same slices as in figure 15. Please notice that the middle cerebral artery does not appear completely at the top of the brain in the central slice. Data are provided by Ron Kikinis, M.D., Department of Radiology, Brigham and Women's Hospital, Harvard Medical School, Boston, MA.

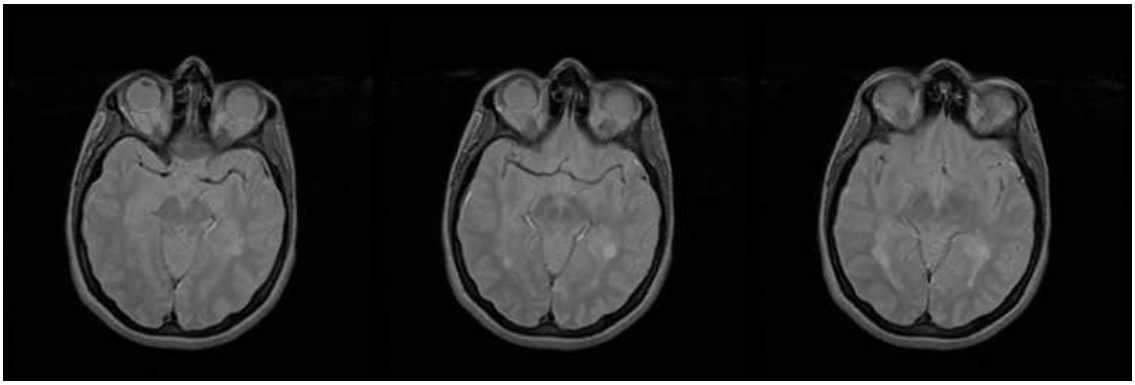

Figure 17: The same three slices of the second data volume after resampling (with the found transformation) as in figure 15. The middle cerebral artery appears now completely in the central slice.

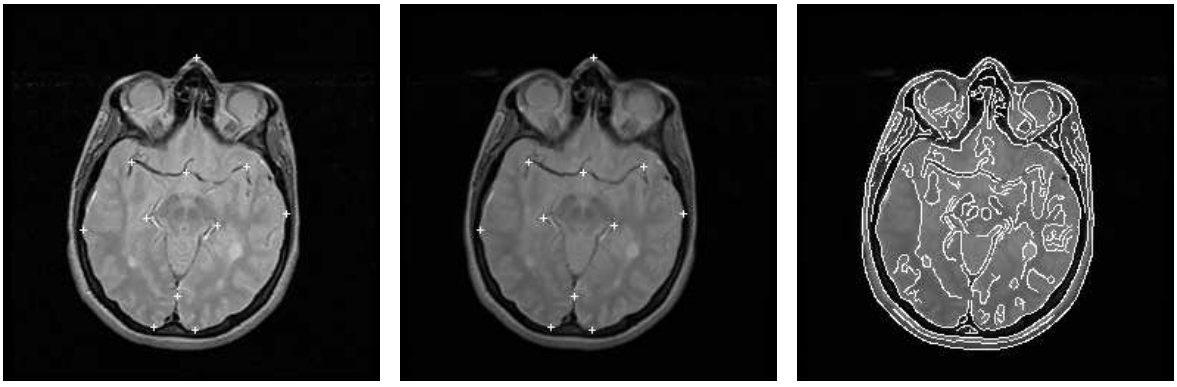

Figure 18: From left to right: the central slice of figure 15 of the first data, the corresponding slice of the second data after resampling (little crosses are showing the same details in both images) and the superimposition of edges extracted from the first image on the second image.

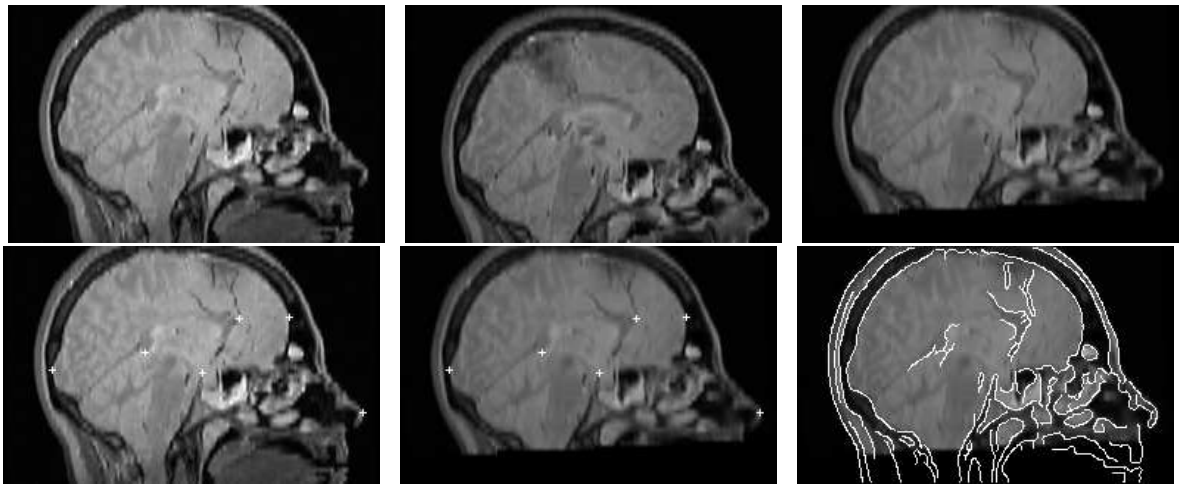

Figure 19: Top, from left to right, we present sagittal slices of respectively the first original scan image, the second original scan image and the second scan image after resampling. Bottom, we present corresponding slices after registration with little crosses pointing out some details and superimposition of the edges of the first image on the second image after resampling. Images seem blurred because of the second resampling we made along the vertical axis in order to obtain quasi-isotropic voxels (for display purpose only).

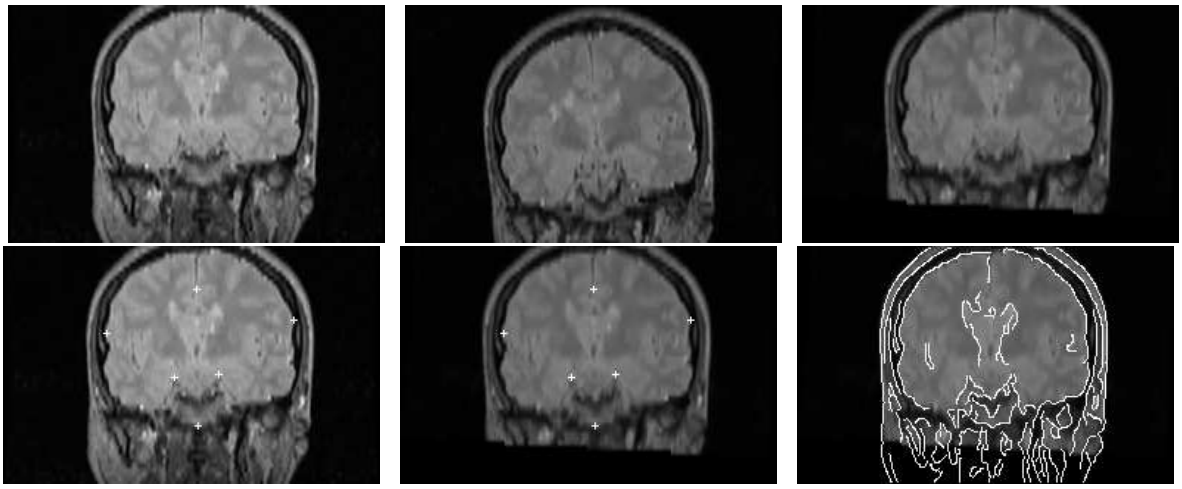

Figure 20: Same as figure 19 with coronal slices.

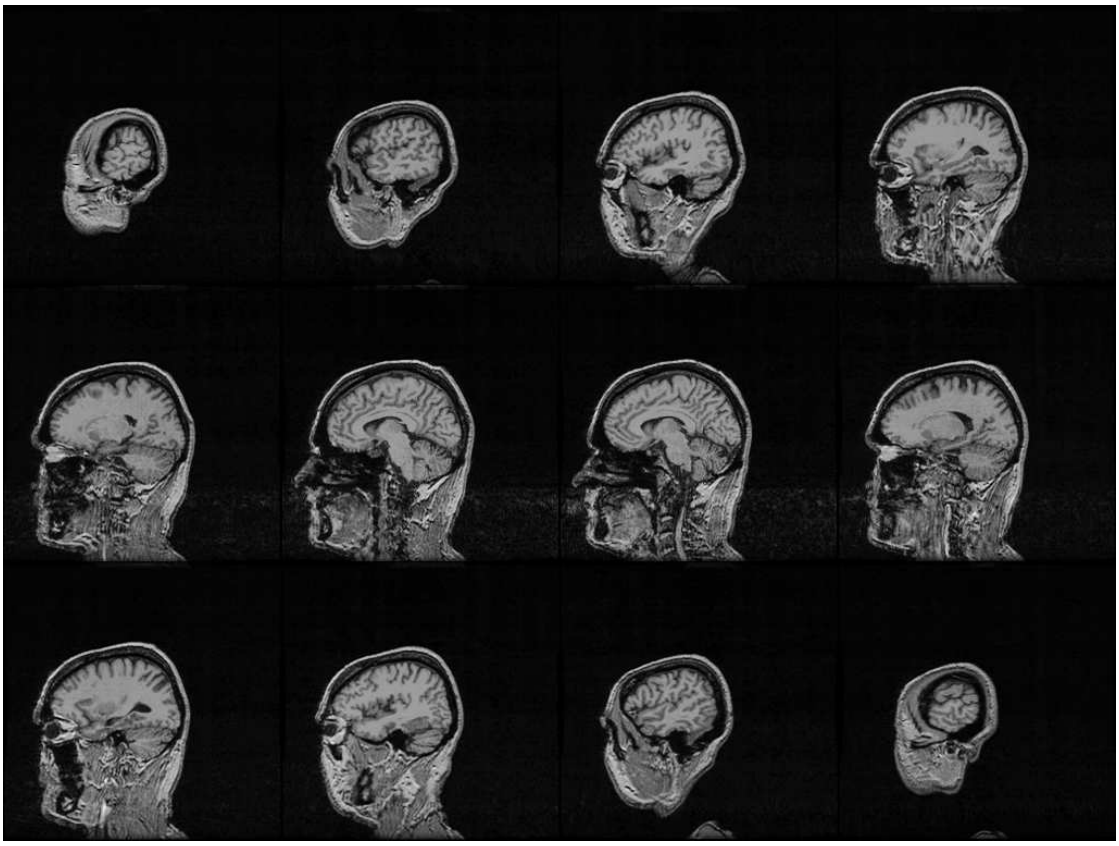

Figure 21: Some slices of the MRI image of the brain. Images are a courtesy of Dr. Jael Travere of Cyceron center (CEA, Caen, France).

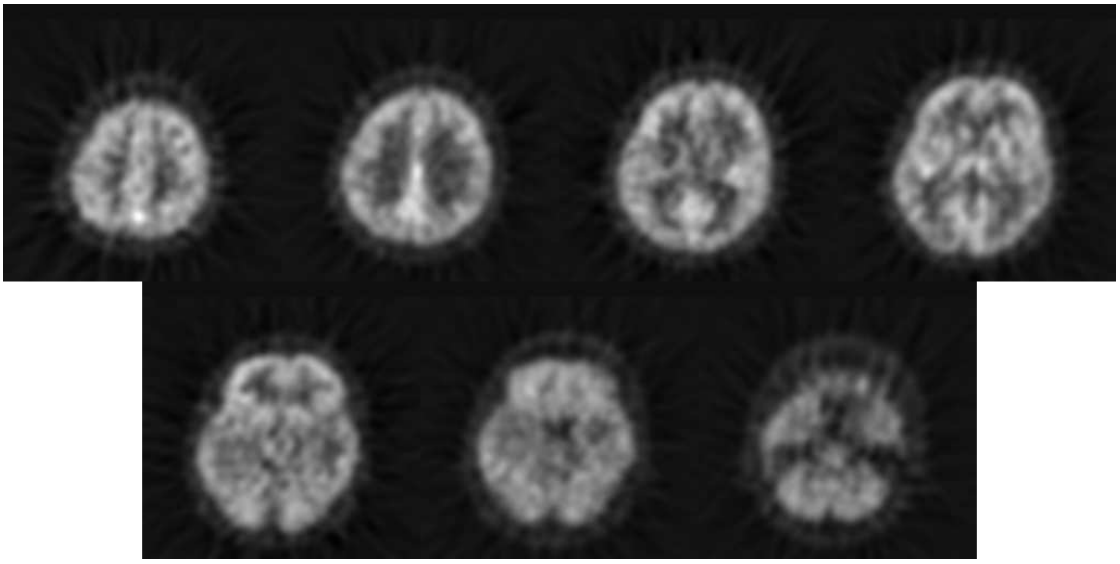

Figure 22: The seven slices of PET data. Images are a courtesy of Dr. Jael Travere of Cyceron center (CEA, Caen, France).

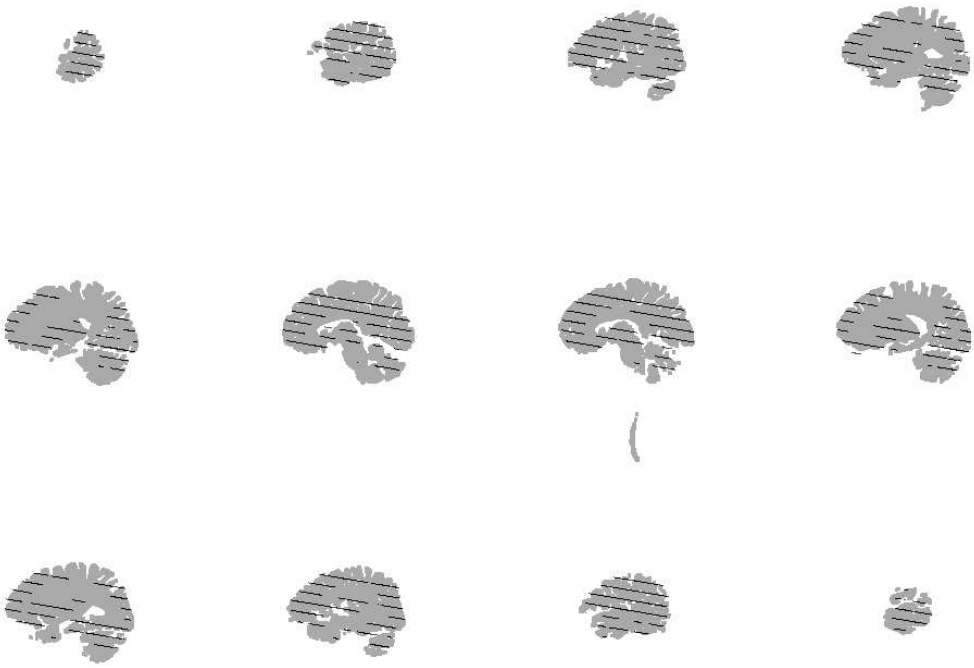

Figure 23: The trace of PET slices on slices of the IRM brain.

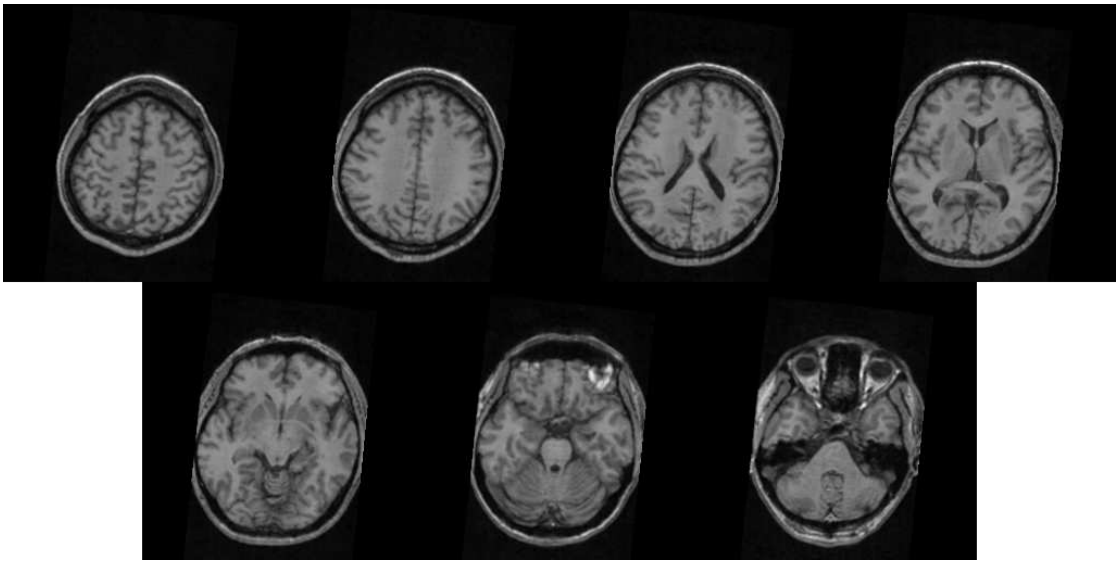

Figure 24: The seven resampled slices in MRI data corresponding to all PET slices.

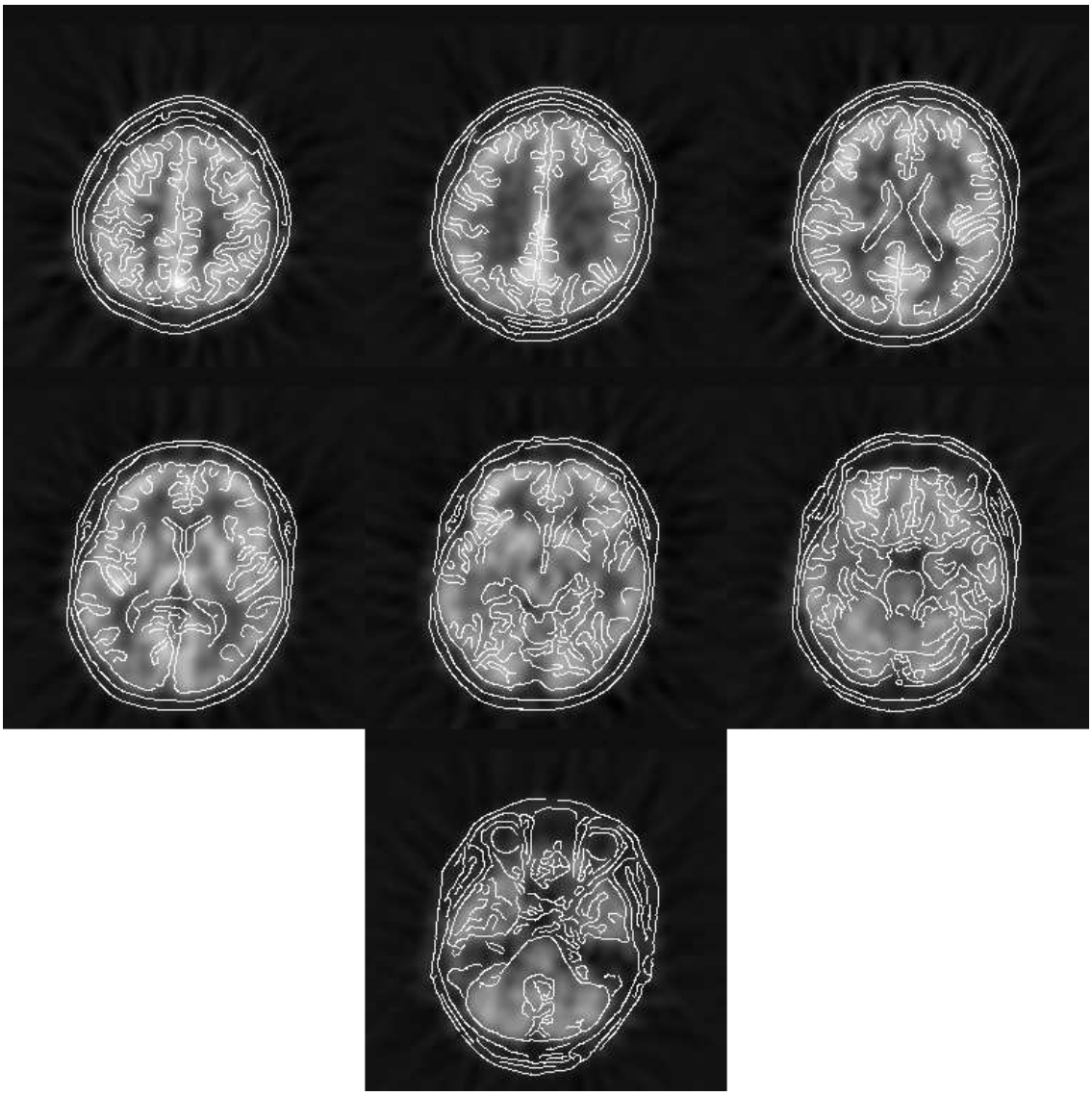

Figure 25: Superimposition of the PET slices with edges extracted from corresponding resampled MRI slices.